Correcting Susceptibility-Induced Distortion in Diffusion-Weighted MRI using Constrained Nonrigid Registration

Chitresh Bhushan*, Justin P. Haldar*, Anand A. Joshi* and Richard M. Leahy*
* Signal and Image Processing Institute, University of Southern California, Los Angeles, CA, USA

***Abstract*—Echo Planar Imaging (EPI) is the standard pulse sequence used in fast diffusion-weighted magnetic resonance imaging (MRI), but is sensitive to susceptibility-induced inhomogeneities in the main B_0 magnetic field. In diffusion MRI of the human head, this leads to geometric distortion of the brain in reconstructed diffusion images and a resulting lack of correspondence with the high-resolution MRI scans that are used to define the subject anatomy. In this study, we propose and test an approach to estimate and correct this distortion using a non-linear registration framework based on mutual-information. We use an anatomical image as the registration-template and constrain the registration using spatial regularization and physics-based information about the characteristics of the distortion, without requiring any additional data collection. Results are shown for simulated and experimental data. The proposed method aligns diffusion images to the anatomical image with an error of 1-3 mm in most brain regions.**

I. Introduction

Diffusion MRI is a non-invasive technique which helps quantify the microstructural characteristics of tissue by in-vivo mapping of diffusion processes [1]. It can provide information about white matter fiber structure in the human brain and can be used to study the brain's anatomical connections [2]. Clinically, diffusion MRI is used for the study and diagnosis of neurological disorders such as stroke [3].

Most diffusion MRI scans use an EPI pulse sequence for data collection. EPI is a popular fast imaging technique, but EPI images are well-known to have localized geometric distortions caused by inhomogeneities in the main magnetic field (B_0) [4], [5], [6]. This distortion is most significant near the boundaries separating air, bone, and soft tissues, where there are large differences in magnetic susceptibility [6], [7]. Geometric image distortion is problematic because anatomical information is frequently used to guide the analysis of diffusion images, and this information is obtained by mapping the diffusion images to anatomical T_1-weighted images. However, since the anatomical images do not use EPI and do not contain geometric distortions, the distortions in the diffusion data can lead to misalignment with the anatomical images by several millimeters, which can limit the accuracy of image analysis in the affected regions[6], [8], [9]. In addition, uncorrected distortion can also lead to unreliable tractography [8].

Most approaches to distortion correction rely on acquiring additional data to provide an accurate model of the distortion. This additional data may include direct mapping of the B_0 field inhomogeneity (also known as a field map) [10], [5], measuring the point spread function [11], or collecting two or more EPI images each with a different phase-encode direction [12], [13]. These methods can be effective, but all require additional acquisitions that are not acquired in a large fraction of imaging studies.

Another class of methods uses the information in undistorted anatomical images to estimate the distortion in EPI images. In these methods, the EPI images are warped to match the anatomical structural images within a non-rigid registration framework [7], [14], [15], [16], [17], [18], [19]. Diffusion images, however, have very different contrast than the standard anatomical scans to which they are registered. This necessitates the use of either a preprocessing step to ensure that the images are similar enough to be registered using pixel-wise differences [14], [15], [16], [17], or optimization metrics such as mutual information (MI) that are insensitive to differences in image contrast [7], [18], [19].

In this work, we propose and evaluate a technique to correct the distortion in diffusion-weighted images using constrained non-rigid registration and MI. This approach only requires the diffusion images and an undistorted anatomical image, without the need for any additional acquisition. Due to the nature of susceptibility-induced distortion [4], we constrain the deformation in two ways. First, we allow deformations only along the phase-encoding direction of the diffusion images. Second, we constrain the deformation to be smooth by adding spatial regularization. During registration, we also account for the localized accumulation and dispersion of the MR signals resulting from distortion by modifying the intensity of the diffusion images. Within the registration framework, the anatomical T_1-weighted image is the template while the diffusion images are warped to match the template.

Similar techniques have been used previously to correct EPI distortion. Studholme et al. [7] used MI with physics-

This study is supported by NIH grants P41 RR013642 and R01 NS074980

based constraints (but no spatial regularization) to correct functional MR images. Others [18], [19] have used spatial regularization (but no physics-constraints) to correct EPI diffusion images. Our approach combines these two constraints to obtain superior results to using either one individually.

This paper is organized as follows. Section II describes the characteristics of geometric distortion in EPI images. Section III describes our proposed registration framework for correcting this distortion. Section IV presents results on simulated and experimental data. Finally, discussion and conclusions are presented in Section V.

II. Distortion in Echo Planar Imaging

EPI is a multi-slice method, in which a 3D image is generated by compositing a series of consecutive 2D images of different imaging planes (slices). Standard MRI encodes each of these 2D slices by manipulating magnetic gradient fields to create a linear correspondence between spatial position in the image and the Fourier-domain frequency of the measured data. B_0 field inhomogeneity disrupts this linear correspondence, such that each slice ρ_e in a standard EPI image is approximately related to its ideal, undistorted version ρ according to the following relationship [7]:

$$\rho(x,y) = |J(x,y)|\ \rho_e(x_e,y_e) \tag{1}$$

where the EPI coordinate (x_e, y_e) is related to the undistorted coordinate (x, y) by

$$x_e = x + \frac{\Delta B_0(x,y)}{G_x} \tag{2}$$

$$y_e = y + \frac{\Delta B_0(x,y)}{G_y}\frac{T_{es}}{\tau} \tag{3}$$

and $|J(x,y)|$ is the Jacobian of the coordinate transformation from undistorted space to distorted EPI space, computed at the undistorted coordinates. This Jacobian term reflects intensity changes in the EPI images that result from the distortion. In this description, we have assumed that x and y are the EPI readout and phase-encoding directions respectively. Here, $\Delta B_0(x,y)$ is the field inhomogeneity, G_x and G_y are the amplitudes of the readout and phase-encode gradients respectively, T_{es} is the echo spacing and τ is the duration of the phase-encode gradient.

Equations (2) and (3) show that the distortion is present in both the readout and phase-encode direction. The term $\frac{T_{es}}{\tau}$ in (3) scales the distortion in the phase-encode direction, typically by an order of magnitude more than distortion in the readout direction. In real scenarios, the distortion in the readout direction is generally sub-millimeter, while the distortion could reach 10-15 millimeters in affected areas along the phase-encoding direction. Hence, similar to much of the existing literature on EPI distortion correction (e.g. [7], [19]), we neglect the distortion along the readout direction by assuming that $x_e = x$ and that

$$|J(x,y)| \approx \frac{\partial y_e}{\partial y}. \tag{4}$$

III. Proposed Framework

The correction of a distorted EPI image F_e using the anatomical image F_a involves (a) estimation of the deformation and (b) correction of intensities using the estimated deformation. The deformation is represented by a transformation $\phi : \underline{X}_a \mapsto \underline{X}_e$ that maps EPI coordinates $\underline{X}_e$ to anatomical image coordinates $\underline{X}_a = [x_a, y_a, z_a]$. Using (1) and (4) we can express the corrected EPI image F_c in the anatomical image coordinates as

$$\begin{aligned} F_c(\underline{X}_a) &\approx F_e(\phi(\underline{X}_a))\ \frac{\partial\, \underline{X}_{e,y}}{\partial y_a} \\ &\approx F_e(\phi(\underline{X}_a))\ \frac{\partial\, \phi_y(\underline{X}_a)}{\partial y_a} \end{aligned} \tag{5}$$

where $\underline{X}_{e,y}$ and $\phi_y(\underline{X}_a)$ represent the y-coordinate of the EPI image, and transformation respectively.

Our proposed method seeks to correct image distortion by optimizing the following cost function

$$\phi = \arg\min_{\phi} \Big(- I(F_a; F_c) + \alpha\, \mathcal{R}(\phi) \Big) \tag{6}$$

where ϕ is the spatial warping operator, $I(F_a; F_c)$ is an energy term that encourages correspondence between the warped image F_c and the target image F_a, $\mathcal{R}(\phi)$ is a regularization term explained later, and α is an experimentally-tuned regularization parameter.

In our implementation, we choose $I(F_a; F_c)$ to be the normalized mutual information (NMI) between F_a and F_c. We use normalized mutual information (NMI) as the measure of image alignment. Mutual information (MI) is a measure of information shared between two random variables (images in our case). Since the diffusion and structural images both originate from the same subject, it is expected that the images will have the maximum shared information when they are correctly aligned, even if the images have very different contrast [20], [21]. However, Studholme et al. [22] showed that MI is sensitive to the overlap between the two images, which can result in less accurate registration. They proposed NMI as a 'normalized' measure which is less sensitive to changes in overlap. The NMI of F_a and F_c is given by

$$I(F_a; F_c) = \frac{H(F_a) + H(F_c)}{H(F_a, F_c)} = \frac{-B(\phi)}{-A(\phi)} \tag{7}$$

where $H(F_a)$ and $H(F_c)$ are the marginal entropies of the images and $H(F_a, F_c)$ is the joint entropy. These entropies are computed from the joint probability density $p(m, n)$ of

the images as:

$$H(F_a, F_c) = -\sum_{m \in F_a} \sum_{n \in F_c} p(m,n) \log\left(p(m,n)\right) \quad (8)$$

$$H(F_a) = -\sum_{m \in F_a} p_{F_a}(m) \log\left(p_{F_a}(m)\right) \quad (9)$$

$$H(F_c) = -\sum_{n \in F_c} p_{F_c}(n) \log\left(p_{F_c}(n)\right) \quad (10)$$

where the marginal probabilities of F_a and F_c, respectively, and are computed by integration of the joint density.

We model the transformation $\phi(\underline{X}_a)$ as a sum of two separate transformations – a rigid transformation $\phi_R(\underline{X}_a)$ due to physical movement and differences in image orientation, and a non-rigid transformation $\phi_{\Delta B_0}(\underline{X}_a)$ due to the B_0 field inhomogeneities:

$$\phi(\underline{X}_a) = \phi_R(\underline{X}_a) + \phi_{\Delta B_0}(\underline{X}_a) \quad (11)$$

We model the non-rigid deformation as a 3D free-form deformation (FFD) based on cubic B-splines [23], [24], which ensures that the transformation is a smooth and locally controlled transformation. We parametrize FFD by the coefficient of set of uniformly spaced control points on a 3D grid. The position of the $(i,j,k)^{\text{th}}$ control points are expressed as $\underline{\Phi}_{ijk}$. In particular, the deformation is described by the outer product of 1D cubic B-splines:

$$\begin{aligned}\phi_{\Delta B_0}(\underline{X}_a) &= \phi_{\Delta B_0}(x_a, y_a, z_a) \quad (12)\\ &= \sum_{i,j,k} \underline{\Phi}_{ijk}\, \mathcal{B}\left(\frac{x_a}{\delta} - i\right) \mathcal{B}\left(\frac{y_a}{\delta} - j\right) \mathcal{B}\left(\frac{z_a}{\delta} - k\right)\end{aligned}$$

where $\mathcal{B}$ is the cubic B-spline kernel [25] and δ is the spacing between the control points in all the directions. uniform spacing δ. We use a single layer of phantom control-points around the boundary to make the deformation well-behaved by interpolating the end control-points [25]. In order to constrain the deformations to only exist along the phase-encode direction, the control points are constrained to move only along the y-coordinate while solving eq.(6). So, the only registration parameters are the y-coordinates of the control points.

In contrast to Studholme et al. [7], we have also included a regularization term $\mathcal{R}(\phi)$ to help stabilize the registration, since we have observed that the registration is otherwise sensitive and prone to over-fitting. Such sensitivity is expected because MI-based similarity measures are based on the joint intensity distribution of the images, but lack spatial location information. This makes MI-based measures unreliable for common MR images with spatially-smooth intensity variations, in which the intensities of neighboring voxels are not independent [26], [27], [28]. Our choice of regularization function is based on the fact that the magnetic field inhomogeneity variations are governed by Maxwell's equations and will generally be smooth. Hence, we used the 3D equivalent of the 2D bending energy of a thin-metal plate for regularization as given by [29]. This regularization ensures the smoothness and invertibility of the transformation and does not penalize any rigid transformations. The resulting regularization term is:

$$\begin{aligned}\mathcal{R}(\phi) = \int_{x,y,z} &\left(\frac{\partial^2\phi}{\partial x^2}\right)^2 + \left(\frac{\partial^2\phi}{\partial y^2}\right)^2 + \left(\frac{\partial^2\phi}{\partial z^2}\right)^2 \quad (13)\\ &+ 2\left(\frac{\partial^2\phi}{\partial xy}\right)^2 + 2\left(\frac{\partial^2\phi}{\partial yz}\right)^2 + 2\left(\frac{\partial^2\phi}{\partial xz}\right)^2 \mathrm{d}x\,\mathrm{d}y\,\mathrm{d}z\end{aligned}$$

To ensure that (6) is a continuous and differentiable function of the registration, we estimate a continuous joint image histogram using a separable Parzen window approach [30]. The histogram takes the form

$$p(m,n) = \frac{1}{\text{Card}(V)} \sum_{\underline{X}_a \in V} h(m - F_a(\underline{X}_a)) h(n - F_c(\underline{X}_a)) \quad (14)$$

where V is the region of overlap and $h(t)$ is a Parzen-window (chosen to be a cubic B-spline in our implementation). A continuous joint histogram allows us to compute the derivative of our cost function analytically. Compared to numerically-computed gradients, analytical gradients are more accurate and thus can improve algorithm performance.

Our choice of the cubic B-spline as the Parzen window $h(t)$ is motivated by its partition of unity property and its local support property [25]. While local support helps to reduce computation, the partition of unity plays an important role in simplifying the expressions for the marginal density and the analytical gradient (15). Similar to [31], [32], we computed the expression for the partial derivative of the mutual information with respect to the registration parameters (y-coordinate of the $(i,j,k)^{\text{th}}$ control point) in our 1D non-rigid framework as

$$\begin{aligned}\frac{\partial I(F_a; F_c)}{\partial\, \underline{\Phi}_{ijk,y}} = \alpha \sum_{m,n} &\left(\frac{\log p_{F_c}(n)}{A(\phi)} - \frac{B(\phi) \log p(m,n)}{A^2(\phi)}\right) \quad (15)\\ &\left(\sum_{\underline{X}_a \in V} h(m - F_a(\underline{X}_a))\, \frac{\mathrm{d}h(t)}{\mathrm{d}t}\bigg|_{t = n - F_c(\underline{X}_a)}\, \frac{-\partial F_c(\underline{X}_a)}{\partial\, \underline{\Phi}_{ijk,y}}\right)\end{aligned}$$

where $A(\phi)$ and $B(\phi)$ are expressed in (7), $\alpha = 1/\text{Card}(V)$, and

$$\begin{aligned}\frac{\partial F_c(\underline{X}_a)}{\partial\, \underline{\Phi}_{ijk,y}} = &F_e(\phi(\underline{X}_a)) \left(\frac{\mathcal{B}(u)\,\mathcal{B}(w)}{\delta}\, \frac{\partial \mathcal{B}(v)}{\partial v}\bigg|_{\underline{X}_a, \underline{\Phi}_{ijk}}\right) \quad (16)\\ &+ \frac{\partial \phi_y(\underline{X}_a)}{\partial y}\, \frac{\partial F_e(\phi(\underline{X}_a))}{\partial y} \left(\mathcal{B}(u)\mathcal{B}(v)\mathcal{B}(w)\bigg|_{\underline{X}_a, \underline{\Phi}_{ijk}}\right)\end{aligned}$$

where δ is the spacing of B-spline control points, and $u = \left(\frac{x_a}{\delta} - i\right)$, $v = \left(\frac{y_a}{\delta} - j\right)$, $w = \left(\frac{z_a}{\delta} - k\right)$. Equation (16) is derived by using (5) and (12). Detailed steps of the derivation of (15) from (7) are given in [31].

Implementation

The whole registration framework was implemented in a multi-resolution pyramid to help avoid local minima [31]. The input images were initially blurred using a Gaussian

smoothing kernel and down-sampled to a coarse resolution. The B-spline control points were initially separated by 30 mm to estimate larger global deformation. The rigid part of the transformation ϕ_R in (11) was initially estimated using rigid registration with MI as described in [22]. Then the non-rigid part of the transformation $\phi_{\Delta B_0}$ was estimated as described above. After performing the registration on a coarse resolution grid, the registration grid was iteratively refined until the number of grid points matched the initial resolution of the images. Each grid refinement was associated with the addition of new B-spline control points, which was performed using the Lane-Riesenfeld Algorithm [33], between existing control points to effectively reduce the spacing between them. This helps to capture the detailed deformation at a finer resolution. A total of four grid refinement steps were used. We used a simple gradient-descent method with decreasing step size to optimize our cost function.

Image interpolation is a necessary component of image registration methods, and it's been previously established that the choice of interpolation method has important consequences for the performance of MI-based registration algorithms [34], [35]. A traditional approach is to use trilinear interpolation, though it has been shown that this biases the registration results due to the blurring effect of the interpolation on the original image [34]. Another alternative is to use nearest-neighbor (NN) interpolation with random jitter to avoid the problems with trilinear interpolation [35]. However, we found that NN interpolation was ineffective for this problem context, since the deformations in diffusion MRI are sub-voxel and thus not captured by NN interpolation in many image regions. After further experimentation, we chose to use trilinear interpolation, but computed the joint histogram based on an oversampled image grid, which substantially reduces the bias in MI-based methods. In this work we sampled all the images on a grid three times denser than the original grid to reduce interpolation artifacts.

IV. Results

A. Simulation

For simulation, we acquired a standard anatomical MPRAGE brain image on a 3T Siemens Magnetom TrioTim scanner. The MPRAGE scan (TE=3.09ms, TR=2530ms, 1x1x1 mm^3 resolution) was used as the registration template. We also acquired an undistorted T_2-weighted scan (TE=88ms, TR=10000ms) at a resolution of 0.8x0.8x3.5 mm, which we used as a gold standard from which we simulated a distorted T_2-weighted EPI image. The EPI distortion model used for the simulation was generated from a real B_0 field inhomogeneity map acquired during the same scan session as the undistorted MPRAGE and T2-weighted images. The field map was estimated from two gradient echo images with different echo times [36], TE=10.00ms and 12.46ms (TR=1300ms for both), at a resolution of 2.0x2.0x2.0 mm^3. Field map estimation

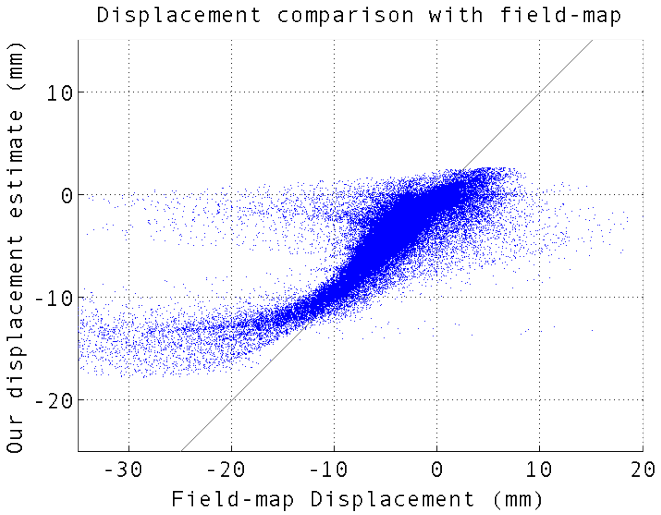

Fig. 1: Scatter plot of our displacement estimate vs the field map displacement for simulated EPI image.

was performed using a simplified version of the regularized estimation framework and graph-cut algorithm described in [37]. All the scans were sampled on the sampling grid of the field map for simulation. The T_2-weighted scan was then distorted using the estimated field map to model the non-ideal Fourier-domain phase accumulation that leads to geometric distortion in EPI images, as described in [4], [7]. This distorted image was then used as the 'simulated' EPI image for the whole sequence. For the purposes of simulation we set the parameters such that the effective distortion was similar to the distortion we observe in real diffusion images. The spatial coordinate transform derived from the field map was also used as a gold standard for the evaluation of our non-rigid registration approach.

We compared the displacement estimated by our method to that computed by the field map in Figs. 1 and 2. If our estimated coordinate transform was estimated perfectly, we would expect all of the data points to lie along a 45-degree line in the scatter plot shown in Fig. 1. Our estimated displacement follows the 45-degree line closely for most of the voxels, although there are some deviations. Fig. 2 shows the comparison of the estimated displacement using our method to the gold standard. The absolute value of the gold standard displacement (in mm) is shown in Fig. 2a, while the absolute error of our displacement estimate is shown in Fig. 2b. From the plots we can see that our displacement estimate is close to the gold standard displacement, within 1-2 millimeters, except in areas lying right next to the frontal sinuses (for which substantial susceptibility changes lead to large variations in the B_0 field and large image distortions). The large amount of distortion in this area makes the signal recovery and distortion correction particularly challenging. Most of the voxels whose estimates are off the 45-degree line in Fig. 1 lie in this troublesome area.

Fig. 3 and Fig. 4 show two slices of the simulated EPI

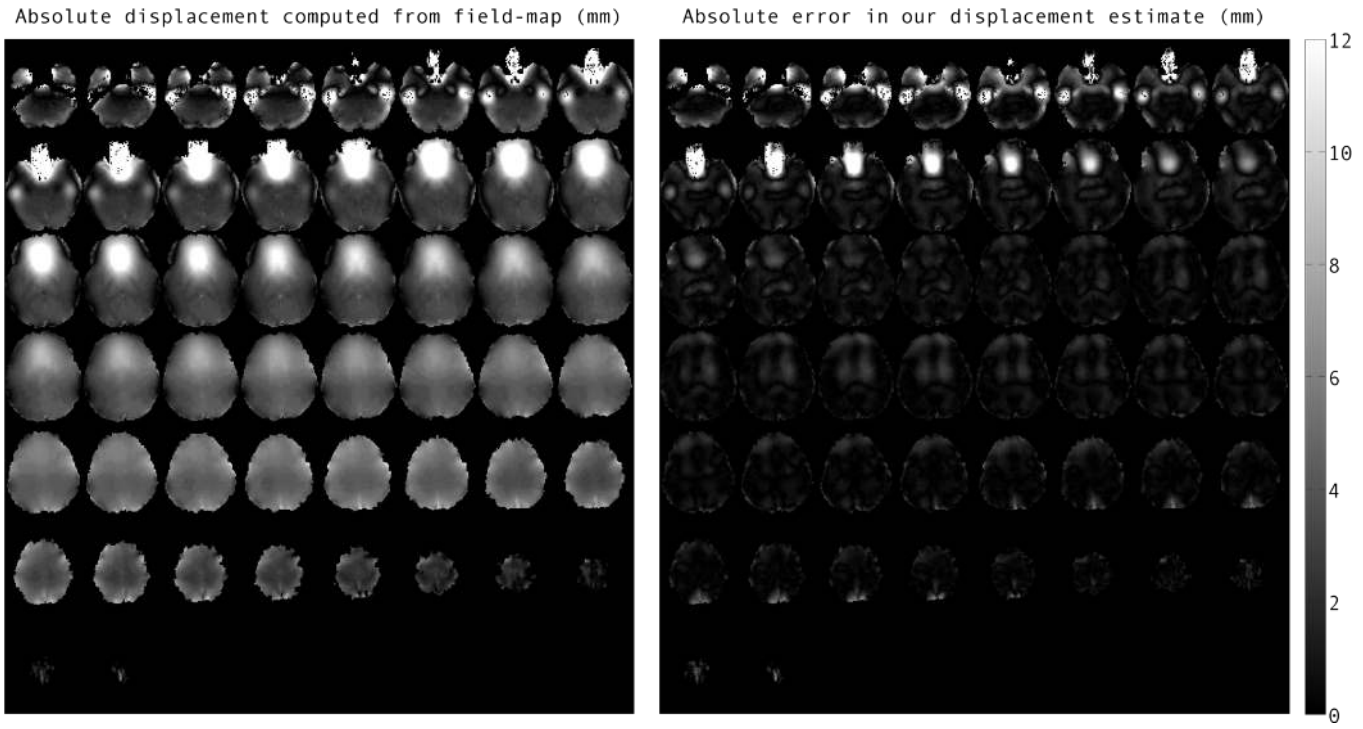

(a) (b)

Fig. 2: Mosaic images showing comparison of the estimated displacements for simulated-EPI image at different slices. (a) Absolute displacement computed using the field map, (b) Error in our displacement estimate (absolute difference between our displacement estimate and field map displacement). The values are reported in millimeters.

images before and after correction using our registration framework. The simulated EPI images are much better aligned with the anatomical MPRAGE image after distortion correction.

B. Imaging experiment

We also tested our approach on a real diffusion-weighted EPI data set. A 64-direction diffusion (single-shot EPI) scan (TE=88ms, TR=10000ms, b=1000s/mm^2) was acquired at a resolution of 2.0x2.0x2.0 mm^3. A standard MPRAGE image was also acquired to be used as the registration template (using the same parameters as in the simulation), and a B_0 field map was also acquired as described previously to provide a gold standard for the geometric distortion.

The proposed algorithm was used to correct the distorted diffusion data. Since all the diffusion weighted images suffer from same static field inhomogeneity, we used just one image, the T_2-weighted b=0 image, to estimate the distortion. Among all the diffusion images, the b=0 has image structure that is the most similar to the structure observed in MPRAGE images. Fig. 5 shows a few slices of the b=0 image before and after the correction, overlaid with an edge-map derived from the MPRAGE image. As expected, the distortions in frontal lobe regions are particularly large, due to the presence of the frontal sinuses, but that our proposed correction framework aligns these and other image regions more accurately.

We also compared our displacement estimates with those derived from the field map in Fig. 6. It can been seen that our approach estimates the displacements within an error of 1-2 millimeters except in areas near the frontal sinuses. The scatter plot in Fig. 7 shows that displacements of most of the voxels in our estimate follow the 45-degree line.

Furthermore, we studied the effect of distortion correction on diffusion measures like Fractional Anisotropy (FA) which are widely used in many studies. We estimated the deformation in the b=0 image using our proposed method and corrected the remaining diffusion images using the same deformation field. The corrected set of diffusion images were then used to estimate the diffusion tensors at each voxel. FA images were generated from the eigenvalues and eigenvectors of the estimated tensors. Fig. 8 shows FA images before and after the correction overlaid with the edge-map of MPRAGE. It can be clearly seen that the white matter regions are much better aligned after correction, especially in frontal areas near the ventricles.

V. Discussion & Conclusion

In this paper, we addressed the common problem of distortion in images acquired using EPI sequences. We proposed a method which does not require extra data

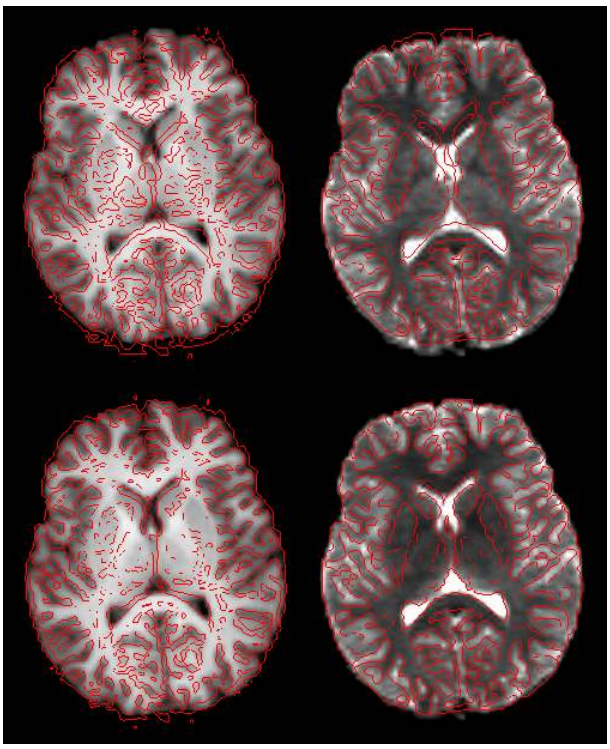

Fig. 3: Overlay of an axial slice before and after correction of the distortion in simulated EPI sequence. The top row shows the images before distortion correction, while the bottom row shows the images after correction. The left column shows the MPRAGE overlaid with the edge-map (in red) generated from the simulated EPI image, while the right column shows the simulated EPI image overlaid with an edge-map generated from the MPRAGE.

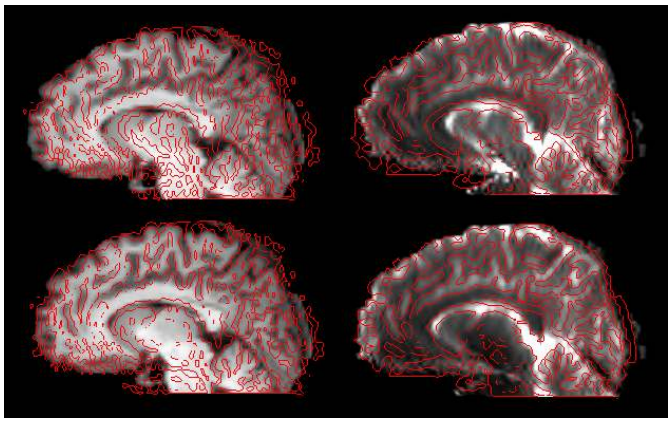

Fig. 4: Overlay of a sagittal slice before and after correction of the distortion in simulated EPI sequence. Images are ordered as described in Fig. 3.

acquisition. Instead, we used an undistorted anatomical image, which is collected to accompany most diffusion data sets, in a non-rigid MI-based registration framework to estimate the distortion. We used regularization and the physics of EPI distortion to constrain the registration process. We demonstrated that proposed approach accurately aligns the diffusion images to the anatomical image. Though we presented the results using a diffusion experiment, the technique remains general and could also be used with a range of other EPI-based acquisitions.

Despite having generally good performance, the proposed technique also has some limitations. In particular, the proposed method cannot recover the image structure that is lost when substantial image distortions lead to the superposition of image information from distinct spatial locations. This limitation can be observed in severely distorted regions like the lower frontal regions of the brain. However, this limitation is also present in correction methods that directly acquire a B_0 field map. Furthermore, in some areas near air/tissue boundaries the main magnetic field changes very rapidly resulting in severely distorted images. These rapid changes cannot be modeled with a small number of B-spline control points. One approach to address this would be to increase the density of control points in severely distorted areas.

In conclusion, the proposed technique shows an improvement in the alignment of diffusion EPI images to the anatomical images over traditional affine and rigid registration technique without need of field map acquisition. This can be particularly useful for diffusion data which has been already acquired without field maps. The results so far indicates that the technique could be useful for many studies in brain imaging.

References

[1] D. K. Jones, *Diffusion MRI: Theory, Methods, and Applications*. Oxford University Press, Inc., 2011.

[2] H. Johansen-Berg and T. E. Behrens, *Diffusion MRI: from Quantitative Measurement to in-vivo Neuroanatomy*. Academic Press, 2009.

[3] K. Kantarci, R. Avula, M. Senjem, A. Samikoglu, B. Zhang, S. Weigand, S. Przybelski, H. Edmonson, P. Vemuri, D. Knopman, T. Ferman, B. Boeve, R. Petersen, and C. Jack, "Dementia with Lewy bodies and Alzheimer disease: Neurodegenerative patterns characterized by DTI," *Neurology*, vol. 74, no. 22, pp. 1814–1821, 2010.

[4] J. L. R. Andersson and S. Skare, "Image distortion and its correction in diffusion MRI," in *Diffusion MRI: Theory, Methods, and Applications* (D. K. Jones, ed.), 2010.

[5] P. Jezzard and R. S. Balaban, "Correction for geometric distortion in echo planar images from B_0 field variations," *Magnetic Resonance in Medicine*, vol. 34, no. 1, pp. 65–73, 1995.

[6] D. K. Jones and M. Cercignani, "Twenty-five pitfalls in the analysis of diffusion MRI data," *NMR in Biomedicine*, vol. 23, no. 7, pp. 803–820, 2010.

[7] C. Studholme, R. T. Constable, and J. S. Duncan, "Accurate alignment of functional EPI data to anatomical MRI using a physics-based distortion model," *IEEE Transactions on Medical Imaging*, vol. 19, pp. 1115 –1127, nov. 2000.

[8] M. O. Irfanoglu, L. Walker, J. Sarlls, S. Marenco, and C. Pierpaoli, "Effects of image distortions originating from susceptibility variations and concomitant fields on diffusion MRI tractography results," *NeuroImage*, vol. 61, no. 1, pp. 275 – 288, 2012.

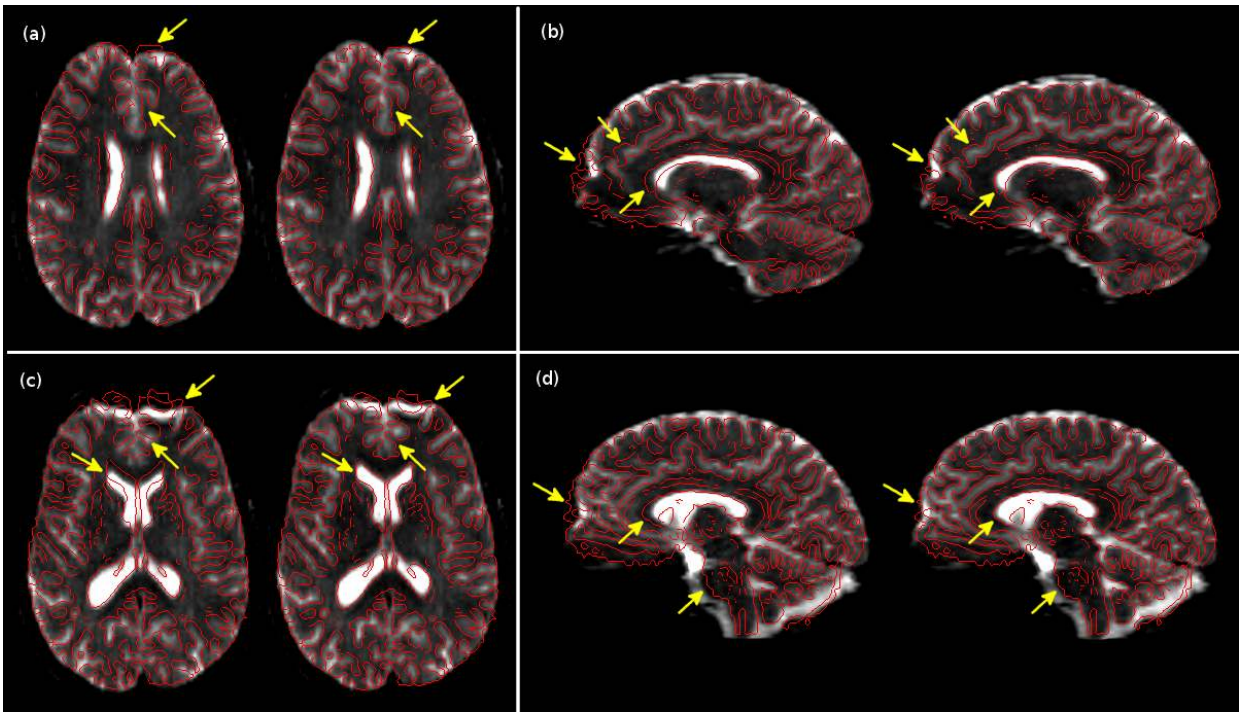

Fig. 5: Results of distortion correction in experimental diffusion data. For each sub-figure, we show (left) the distorted and (right) undistorted b=0 image overlaid with the edge-map generated from the MPRAGE (in red). The arrows indicate a few of the locations where substantial distortions have been corrected.

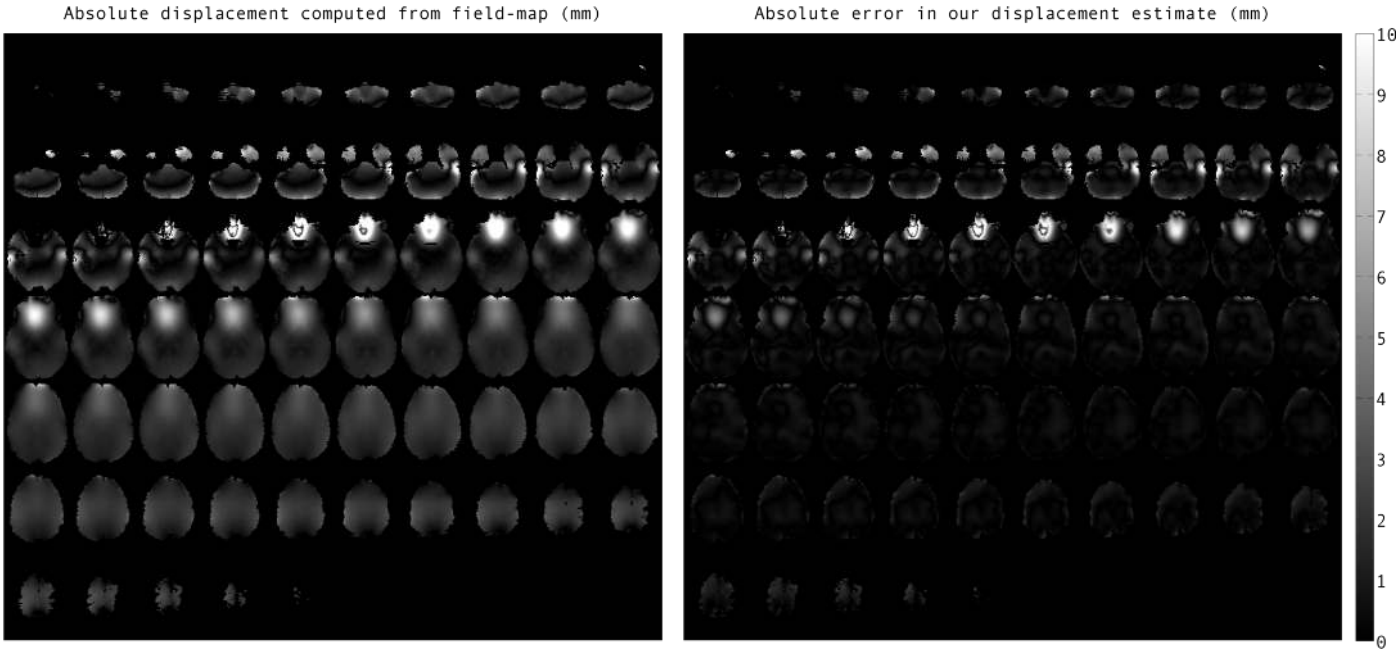

(a) (b)

Fig. 6: Comparison of the estimated displacements with the field-map based 'gold standard' for real diffusion data. (a) Absolute displacements computed using the field map, (b) Error in our displacement estimates (absolute difference between our displacement estimates and the field map displacements).

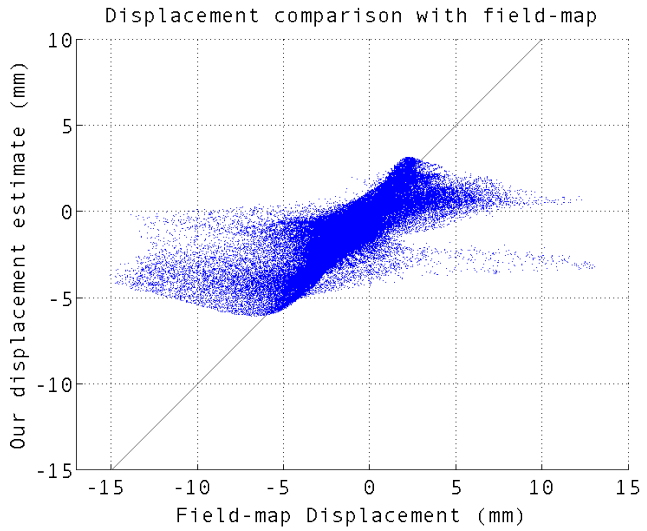

Fig. 7: Scatter plot of our estimated displacement vs the field map displacement for diffusion data.

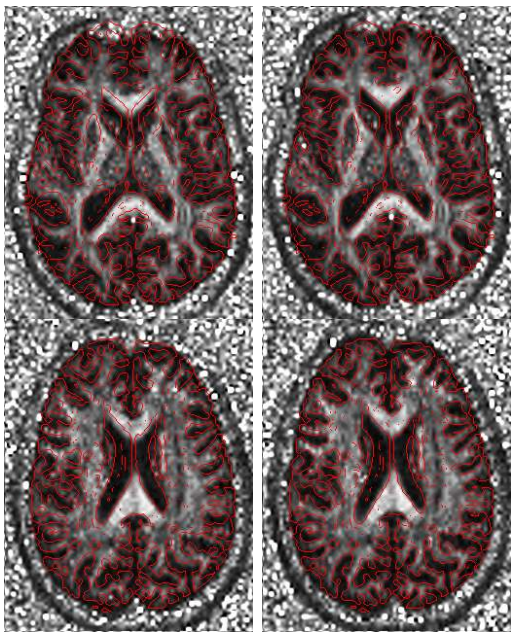

(a) (b)

Fig. 8: FA images before and after the correction of diffusion images. (a) shows different slices of the distorted FA image overlaid by edge-map of MPRAGE. (b) shows the FA image after correction.

[9] K. V. Embleton, H. A. Haroon, D. M. Morris, M. A. L. Ralph, and G. J. Parker, "Distortion correction for diffusion-weighted MRI tractography and fMRI in the temporal lobes," *Human Brain Mapping*, vol. 31, no. 10, pp. 1570–1587, 2010.

[10] R. Weisskoff and T. Davis, "Correcting gross distortion on echo planar images," in *Proceedings of the SMRM 11th Annual Meeting Berlin*, p. 4515, 1992.

[11] H. Zeng and R. T. Constable, "Image distortion correction in EPI: Comparison of field mapping with point spread function mapping," *Magnetic Resonance in Medicine*, vol. 48, no. 1, pp. 137–146, 2002.

[12] R. Bowtell, D. McIntyre, M. Commandre, P. Glover, and P. Mansfield, "Correction of geometric distortion in echo planar images," in *Proceedings of the Society of Magnetic Resonance, San Francisco*, 1994.

[13] J. L. Andersson, S. Skare, and J. Ashburner, "How to correct susceptibility distortions in spin-echo echo-planar images: application to diffusion tensor imaging," *NeuroImage*, vol. 20, no. 2, pp. 870 – 888, 2003.

[14] J. Kybic, P. Thevenaz, A. Nirkko, and M. Unser, "Unwarping of unidirectionally distorted EPI images," *IEEE Transactions on Medical Imaging*, vol. 19, pp. 80 – 93, feb. 2000.

[15] M. Irfanoglu, L. Walker, S. Sammet, C. Pierpaoli, and R. Machiraju, "Susceptibility distortion correction for echo planar images with non-uniform b-spline grid sampling: A diffusion tensor image study," in *Medical Image Computing and Computer-Assisted Intervention 2011* (G. Fichtinger, A. Martel, and T. Peters, eds.), vol. 6892 of *Lecture Notes in Computer Science*, pp. 174–181, Springer Berlin / Heidelberg, 2011.

[16] R. Tao, P. Fletcher, S. Gerber, and R. Whitaker, "A variational image-based approach to the correction of susceptibility artifacts in the alignment of diffusion weighted and structural MRI," in *Information Processing in Medical Imaging* (J. Prince, D. Pham, and K. Myers, eds.), vol. 5636 of *Lecture Notes in Computer Science*, pp. 664–675, Springer Berlin / Heidelberg, 2009.

[17] H. Huang, C. Ceritoglu, X. Li, A. Qiu, M. I. Miller, P. C. van Zijl, and S. Mori, "Correction of B_0 susceptibility induced distortion in diffusion-weighted images using large-deformation diffeomorphic metric mapping," *Magnetic Resonance Imaging*, vol. 26, no. 9, pp. 1294 – 1302, 2008.

[18] X.-F. Yao and Z.-J. Song, "Deformable registration for geometric distortion correction of diffusion tensor imaging," in *Computer Analysis of Images and Patterns* (P. Real, D. Diaz-Pernil, H. Molina-Abril, A. Berciano, and W. Kropatsch, eds.), vol. 6854 of *Lecture Notes in Computer Science*, pp. 545–553, Springer Berlin / Heidelberg, 2011.

[19] M. Wu, L.-C. Chang, L. Walker, H. Lemaitre, A. Barnett, S. Marenco, and C. Pierpaoli, "Comparison of EPI distortion correction methods in diffusion tensor MRI using a novel framework," in *Medical Image Computing and Computer-Assisted Intervention – MICCAI 2008* (D. Metaxas, L. Axel, G. Fichtinger, and G. Székely, eds.), vol. 5242 of *Lecture Notes in Computer Science*, pp. 321–329, Springer Berlin / Heidelberg, 2008.

[20] P. Viola and W. M. Wells, "Alignment by maximization of mutual information," *International Journal of Computer Vision*, vol. 24, pp. 137–154, 1997. 10.1023/A:1007958904918.

[21] F. Maes, A. Collignon, D. Vandermeulen, G. Marchal, and P. Suetens, "Multimodality image registration by maximization of mutual information," *Medical Imaging, IEEE Transactions on*, vol. 16, pp. 187 –198, april 1997.

[22] C. Studholme, D. Hill, and D. J. Hawkes, "An overlap invariant entropy measure of 3D medical image alignment," *Pattern Recognition*, vol. 32, no. 1, pp. 71 – 86, 1999.

[23] M. Holden, "A review of geometric transformations for nonrigid body registration," *IEEE Transactions on Medical Imaging*, vol. 27, pp. 111 –128, jan. 2008.

[24] D. Rueckert, L. Sonoda, C. Hayes, D. Hill, M. Leach, and D. Hawkes, "Nonrigid registration using free-form deformations: application to breast mr images," *IEEE Transactions on Medical Imaging*, vol. 18, pp. 712 –721, aug. 1999.

[25] R. H. Bartels, J. C. Beatty, and B. A. Barsky, *An Introduction to Splines for Use in Computer Graphics & Geometric Modeling.*

San Francisco, CA, USA: Morgan Kaufmann Publishers Inc., 1987.

[26] J. P. Pluim, J. A. Maintz, and M. A. Viergever, "Mutual-information-based registration of medical images: a survey," *IEEE Transactions on Medical Imaging*, vol. 22, pp. 986 –1004, aug. 2003.

[27] D. Rueckert, M. J. Clarkson, D. L. G. Hill, and D. J. Hawkes, "Non-rigid registration using higher-order mutual information," vol. 3979, pp. 438–447, SPIE, 2000.

[28] C. Studholme, D. Hill, and D. Hawkes, "Incorporating connected region labelling into automated image registration using mutual information," in *Proceedings of the Workshop on Mathematical Methods in Biomedical Image Analysis, 1996*, pp. 23 –31, jun 1996.

[29] F. Bookstein, "Principal warps: thin-plate splines and the decomposition of deformations," *IEEE Transactions on Pattern Analysis and Machine Intelligence*, vol. 11, pp. 567 –585, jun 1989.

[30] R. O. Duda, P. E. Hart, and D. G. Stork, *Pattern Classification*, vol. 10. John Wiley and Sons., 2001.

[31] P. Thevenaz and M. Unser, "Optimization of mutual information for multiresolution image registration," *IEEE Transactions on Image Processing*, vol. 9, pp. 2083 – 2099, dec 2000.

[32] R. Xu, Y.-W. Chen, S.-Y. Tang, S. Morikawa, and Y. Kurumi, "Parzen-window based normalized mutual information for medical image registration," *IEICE Transactions on Information and Systems*, vol. E91.D, no. 1, pp. 132–144, 2008.

[33] J. M. Lane and R. F. Riesenfeld, "A theoretical development for the computer generation and display of piecewise polynomial surfaces," *IEEE Transactions on Pattern Analysis and Machine Intelligence*, vol. PAMI-2, pp. 35 –46, jan. 1980.

[34] J. P. Pluim, J. A. Maintz, and M. A. Viergever, "Interpolation artefacts in mutual information-based image registration," *Computer Vision and Image Understanding*, vol. 77, no. 2, pp. 211 – 232, 2000.

[35] J. Tsao, "Interpolation artifacts in multimodality image registration based on maximization of mutual information," *IEEE Transactions on Medical Imaging*, vol. 22, no. 7, pp. 854–864, 2003.

[36] E. Schneider and G. Glover, "Rapid in vivo proton shimming," *Magnetic Resonance in Medicine*, vol. 18, no. 2, pp. 335–347, 1991.

[37] D. Hernando, P. Kellman, J. P. Haldar, and Z.-P. Liang, "Robust water/fat separation in the presence of large field inhomogeneities using a graph cut algorithm," *Magnetic Resonance in Medicine*, vol. 63, no. 1, pp. 79–90, 2010.